Check for updates

Phase-locking of time-delayed attosecond XUV pulse pairs

LISA-MARIE KOLL,[1] LAURA MAIKOWSKI,[1] LORENZ DRESCHER,[2] MARC J. J. VRAKKING,[1] AND TOBIAS WITTING[1,*]

[1] *Max-Born-Institut, Max-Born-Str. 2A, 12489 Berlin, Germany*
[2] *Department of Chemistry, University of California, Berkeley, California 94720, USA*
[*]witting@mbi-berlin.de

Abstract: We present a setup for the generation of phase-locked attosecond extreme ultraviolet (XUV) pulse pairs. The attosecond pulse pairs are generated by high harmonic generation (HHG) driven by two phase-locked near-infrared (NIR) pulses that are produced using an actively stabilized Mach-Zehnder interferometer compatible with near-single cycle pulses. The attosecond XUV pulses can be delayed over a range of 400 fs with a sub-10-as delay jitter. We validate the precision and the accuracy of the setup by XUV optical interferometry and by retrieving the energies of Rydberg states of helium in an XUV pump–NIR probe photoelectron spectroscopy experiment.

1. Introduction

Attosecond pulses have enabled many new insights into atomic, molecular, solid state, and nanoscale physics [1–3]. Most experiments employ a combination of an attosecond pulse train (APT) or an isolated attosecond pulse (IAP) generated via high harmonic generation (HHG) with a low frequency driving pulse, which can lie in the ultraviolet (UV), visible, near infrared (NIR), or infrared spectral range. The observable experimental signal is then recorded as a function of the delay between the APT/IAP and the low-frequency laser field.

In the visible to infrared spectral ranges, multidimensional spectroscopies using phase-locked sequences of multiple femtosecond pulses have become established experimental techniques to explore collective dynamics and correlations in matter [4–13]. By employing sequences of multiple pulses and measuring a non-linear signal as a function of the delays between those pulses, frequency-domain information can be associated with the pump and/or probe laser interaction (by means of a Fourier Transform) and all non-linear optical responses can be measured simultaneously, so that couplings between quantum states can be revealed.

First advances to transfer multidimensional spectroscopy into the attosecond science field have been made by combining an XUV pulse with multiple NIR pulses [14], or by preparing multiple independent XUV sources. Pairs of XUV pulses can be generated either by directly splitting an XUV beam, or by splitting the generating NIR beam with subsequent HHG. The first method was implemented as a Michelson interferometer for VUV pulses by means of transmission gratings by Goulielmakis et al. [15]. In the XUV range, beam splitting can be implemented by a mirror pair. These methods have been used for temporal coherence measurements of HHG radiation [16], attosecond pulse duration measurement by non-linear autocorrelation [17], linear and nonlinear Fourier transform spectroscopy [18,19], and as an approach towards the realization of VUV-XUV pump-probe experiments [20–22]. The generation of an XUV pulse pair by splitting an XUV beam is relatively straightforward and the XUV-XUV delay jitter is intrinsically minimized due to the common-path geometry. However due to the geometric splitting of the XUV beam into two halves by a mirror pair, the quality of the focus that can subsequently be achieved is compromised due to the sharp cut in the spatial profiles and the spatial fringe caused by non-collinearity after the splitting [23].

Phase-locked XUV pulse pairs with a variable delay can also be generated by splitting the NIR driving pulses before the XUV pulse generation by HHG. In the literature a number of implementations are described that accomplish this. Pulse pairs with a delay jitter of 300 zs and a delay range of 120 fs have been generated by LCD based 4f-line polarization pulse shaping [24]. Drawbacks of this method are poor transmission, pixelation and phase wrapping artifacts leading to satellite pulses, and spatio-temporal couplings [25]. Alternatively, two pairs of birefringent wedges can be employed for pulse splitting [26,27]. This approach is limited to >10 cycle pulses, due to the dispersion differences induced by propagation along the $o-$ and $e-$ axes of the birefringent material. Spatial wavefront pulse shaping can be used for dispersion-less high phase stability pulse pair generation [28]. However, this method is restricted to delay ranges of only a few optical cycles.

A straightforward alternative to all of the aforementioned methods is the use of a Michelson or Mach-Zehnder interferometer [29–34]. With this method large delay ranges can easily be implemented, however maintaining a degree of phase-locking that leads, upon HHG, to the generation of phase-locked XUV pulses, is non-trivial.

In the present work, the challenge is to generate two phase-locked attosecond XUV pulses with a variable time delay over a ∼ 400 fs range. For XUV pulses in the 10 to 50 eV range the driving pulses should then have a delay stability of better than 10 as. We accomplish this by the development of a phase-locked, few-cycle compatible Mach-Zehnder interferometer with low and balanced dispersion and equal wavefronts in both interferometer arms. In this paper we present the setup and describe the generation of two phase-locked attosecond pulses. This approach has already been used to prepare a combination of two phase-locked APTs to control entanglement in molecules [35,36].

2. Phase-locked NIR pulse pair generation

A Mach-Zehnder interferometer is constructed to split and delay the NIR pulses into phase-locked pairs of identical pulses (cf. Figure 1). The interferometer is designed to be compatible with few-cycle pulses. The coatings on the 1 mm thick beamsplitters are low-dispersion ultrabroadband coatings (106896, Layertec GmbH) with a reflectivity $R = 50\%$ over a range from 440 to 1020 nm, and with a dispersion <5 fs^2 over this range. The backsides are antireflection-coated to reduce losses and also to provide less unilateral stress to the glass to minimize residual surface bend.

Phase-lock with attosecond precision is achieved by a combination of passive and active stabilization. The interferometer is constructed on the smallest possible footprint with an interferometer arm length of only ∼50 mm. The interferometer breadboard "floats" on Viton o-rings recessed into the underside of the breadboard to decouple the interferometer from laser table vibrations in the 100 Hz range. Arm A contains the time-delay stage (piezo stage PIHera P-620.10L, Physik Instrumente) with a minimum incremental motion of 0.1 nm and a maximum travel range of 60 μm and controls the time-delay $\tau_{\text{XUV-XUV}}$ between the two pulse replicas produced in the interferometer. The retroreflecting mirror pair is mounted on a stainless steel plate to increase the mass and thus shift the resonance frequency below prominent noise sources in the lab. In order to find the zero delay and for extension of the delay range, arm B contains a 21 mm range piezo stick-slip stage (SLC-1730-S, Smaract). A lateral beam offset between arm A and arm B can be introduced and controlled with a second SLC-1730-S stage mounted at a 90 degree angle to the beam axis in arm B. The recombining beamsplitter is mounted onto a piezo mirror mount (Polaris-K05P2, Thorlabs). This allows for very precise overlap of the two NIR beams, as well as the controlled introduction of an angle between the two beams. As illustrated in Fig. 1 this enables collinear as well as non-collinear operation with a controlled setting of the beam lateral positions and tilt angles [37]. This enables control over the angle and the overlap between the two beams in the focus or in the far field.
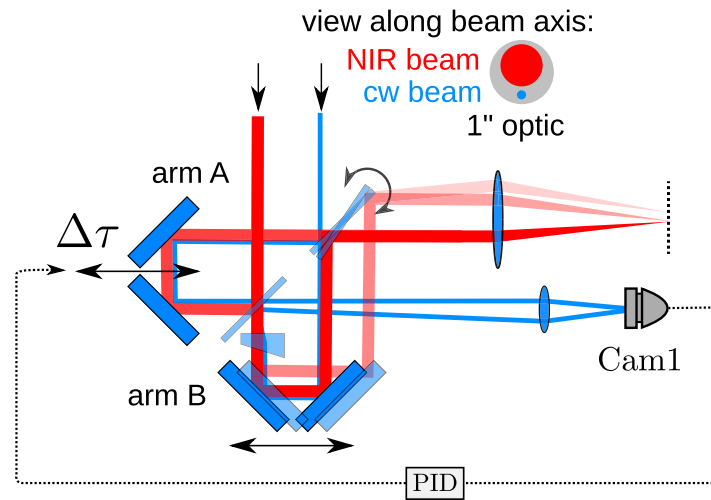
Fig. 1. Mach-Zehnder interferometer for the generation of phase-locked NIR pulse pairs. One NIR pulse can be delayed by a piezo stage in arm A (solid red beam). A translation stage in arm B allows to adjust the lateral beam position and the second beamsplitter can be tilted to adjust the beam tilt angle for non-colinear operation (indicated by the transparent red beam). A beam tilt becomes a lateral beam shift after the focusing element (indicated by the lens) and vice versa. For active phase stabilization a cw laser is co-propagated through the interferometer below the NIR beam (see the view along the beam axis). In arm B a wedge is placed (below the NIR beam) to tilt the cw beam by a fixed angle. This leads to fringes, which are monitored by a CMOS camera (Cam 1). After evaluation of the phase drift, a feedback signal is sent to the delay stage in arm A.

The flexibility to operate in a non-collinear as well as a collinear geometry allows interferometry experiments [38–41] and Fourier transform experiments [29–31,33,34]. The advantage of the non-collinear geometry is the possibility of using two independent non-overlapping HHG sources for two source interferometry. The collinear setup allows to perform Fourier transform spectroscopy experiments with highest interference contrast.

The passive stabilization leads to a short term delay stability of $\sigma = 5$ to 10 as. However, due to air currents and thermal effects (the interferometer consists of various materials with different thermal expansion coefficients), the delay will slowly drift at a rate dependent on environmental conditions (see Fig. 2(a)). Therefore, active phase-stabilization is employed with a frequency stable cw laser as absolute length reference. The cw laser (Cobolt Blues, Hübner Photonics) has a wavelength of 473.36 nm, a <1 MHz linewidth, and a stability of <1 pm (0.001 nm) over 8 hours in typical laboratory conditions ($\pm\,2$ centigrade temperature swing). For successful sampling of XUV spectra up to $E_{max} = 100$ eV ($\rightarrow \lambda_{min} = 12.4$ nm) a minimal stepsize of $\delta\tau_{min} = \lambda_{min}/2c = 20$ as is required according to the Whittaker–Nyquist–Shannon sampling theorem. Therefore we aim for a 1-σ delay jitter better than 10 as, which corresponds to a phase stability of better than 40 mrad for a 473.36 nm cw stabilization laser. With 3 mW average power, $N = 5 \times 10^{12}$ photons are detected per frame (1.5 kHz detection rate), resulting in a phase detection noise of $\delta\phi = \pi/\sqrt{N/2} = 2$ μrad, which is negligible compared to the required 40 mrad phase-stability. At the same time, the accuracy of the delay is guaranteed by the wavelength stability of the 473.36 nm cw laser. For a wavelength error of $\delta\lambda = 1$ pm the delay error amounts to $\Delta\tau\delta\lambda/\lambda = 0.8$ as for a delay range $\Delta\tau$ of 400 fs.

The cw laser beam enters the interferometer through the backside of the recombining beamsplitter and exits through the backside of the first beamsplitter (where the NIR femtosecond
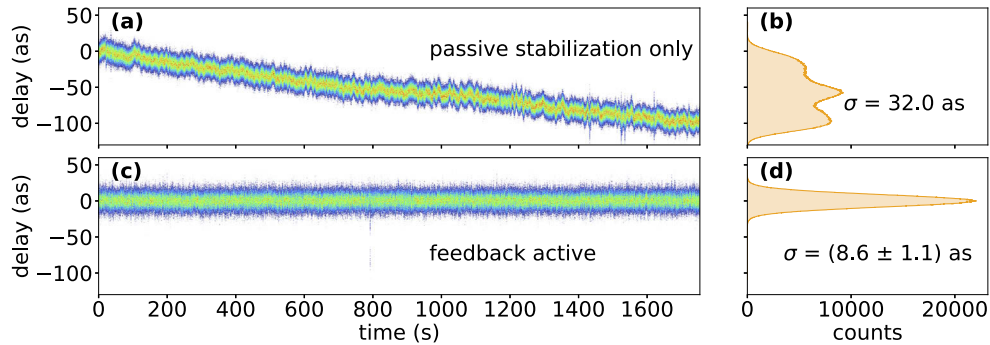
Fig. 2. Optical measurement of the interferometer phase drift using the cw laser. (a) Phase drift of the unstabilized interferometer. (c) Phase drift with active feedback stabilization. (b) and (d) show the phase jitter histograms for the data in (a) and (c).

beam enters). The cw beam is aligned to a height just below the NIR femtosecond beam (see inset in Fig. 1). Both, the cw and the NIR beams reflect off and propagate through the same optics (two beamsplitters, 4 silver mirrors), just at different heights. In arm B a wedge (30 arcmin face angle) is placed just below the femtosecond beam near the recombining beamsplitter to introduce a small angle α between the two cw beams from both interferometer arms, leading to a difference in the x-components of the wavevectors $\Delta k_{x,\text{cw}} = k_{z,\text{cw}} \sin \alpha$, where $k_{z,\text{cw}}$ is along the propagation direction of the cw beam. A lens re-images the plane of the wedge onto a CMOS camera. Tilt fringes are observed, i.e. a $\cos(\phi_\tau + \Delta k_{x,\text{cw}}x)$ spatial modulation of the beam image on the camera, where ϕ_τ is the shift in the phase of the interferogram due to the drift between the two arms of the interferometer. The phase term ϕ_τ is extracted via FFT processing using the Takeda algorithm [42]. Using a fast USB3 CMOS camera combined with readout of a small region of interest (ROI) allows for acquisition and processing speeds of typically 1.5 kHz. From the extracted phase signal we obtain an error-signal (i.e. the difference to a user-defined setpoint) which is fed into a software proportional integral differential (PID) controller. This drives the piezo stage (cf. arm A in Fig. 1) to control the delay. The servo rate is set to 20 Hz to avoid inducing vibrations into the piezo stage. Thanks to the passive stability of the setup we only have to control the slow phase-drift.

To perform time delay scans a requested time delay $\tau_{\text{XUV-XUV}}$ is converted to a phase-value ϕ_τ in radians by: $\phi_\tau = 2\pi \tau_{\text{XUV-XUV}}/T_{\text{cw}}$, with the period of the cw laser T_{cw}. The piezo stage is moved slowly whilst keeping track of the measured phase. Fast acquisition is important here. This way any arbitrary ϕ_τ (containing very large multiples of 2π) can be reached without losing the phase-lock. As the cw laser provides only a phase relative to an arbitrary zero-point, we perform an HHG scan before an experimental run to determine the absolute $\tau_{\text{XUV-XUV}} = 0$ position. The corresponding phase is saved as a reference and an absolute phase-lock with 6 to 9 as rms can be kept for 24 h over multiple days whilst continuously scanning over hundreds of fs range multiple times.

The phase stability is recorded over an extended time using the fringe patterns of the cw laser beam. As seen in Fig. 2(a) the passive stability leads to a short term jitter below 10 as, but the interferometer drifts over many tens of attoseconds within half an hour. Figure 2(b) shows the delay stability data with the active feedback (see section 2.) engaged. The measured residual delay jitter amounts to just (8.6 ± 1.1) as rms, which meets our stability goal of delay jitters below 10 as.

3. Phase-locked XUV pulse pair generation

In the experiment, phase-locked NIR pulses that are obtained from the Mach-Zehnder interferometer described in section 2 are employed to produce a phase-locked pair of XUV pulses, using high-harmonic generation (HHG). To this end, the Mach-Zehnder interferometer described in section 2 is placed in the XUV arm of a two-color XUV+NIR Mach-Zehnder interferometer, where attosecond XUV pulses and NIR pulses that are used in an attosecond XUV+NIR pump-probe experiment are produced with a controllable time delay. The current section 3 describes the complete experimental setup and shows spectral measurements that characterize the performance of the Mach-Zehnder interferometer detailed in section 2. Subsequently, section 4 describes experiments on two-color XUV+NIR ionization of helium that provide a further, independent characterization of the Mach-Zehnder interferometer.

Few-cycle pulses are generated by hollow core fiber pulse compression. Pulses with energies of up to 2 mJ and durations of 28 fs from a Ti:Sapphire laser system (Aurora, Amplitude Technologies) are coupled into a 1 m long fused silica waveguide (1002562, Hilgenberg GmbH) with a core diameter of 340 μm filled with up to 3 bar of neon gas in gradient pressure configuration [43]. The bandwidth is increased up to a full octave. Pulse energies up to 1.4 mJ are obtained after the fiber. Phase compensation is achieved by a combination of double angle chirped mirrors (PC70, Ultrafast Innovations GmbH) [44,45] and fused silica wedges (OA925, Spectra-Physics Femto-Optics). To compensate for the negative third-order dispersion acquired in the non-linear pulse compression scheme [45,46] a 2 mm long *z*-cut potassium dihydrogenphosphate (KDP) crystal is employed. For this experiment the compressed pulses have pulse durations of about 5 fs.

The compressed NIR pulses are sent to a phase-stabilized two-color, XUV+NIR interferometer (Fig. 3(a)). BS1 reflects 20 % of the pulse energy to serve as NIR probe pulse, while the remaining 80 % are used for XUV generation. The XUV and NIR beams are recombined with a drilled mirror (DM in Fig. 3). The NIR pulse can be delayed with respect to the XUV pulses using a stick-slip piezo stage (SLC-1730-LC-ST, Smaract GmbH). To stabilize the delay between the XUV and NIR interferometer arms, a frequency stable 761 nm cw laser (BrixX 761-10, omicron Laser GmbH) is aligned to co-propagate through the interferometer below the NIR beam similar to the way that this was done in section 2. A tilt between the cw beams propagating along both arms is introduced leading to vertically aligned spatial fringes. The fringe pattern is recorded by a CMOS camera and after FFT-processing a feedback signal is generated to actively stabilize the interferometer to a residual delay jitter with a standard deviation $\sigma < 100$ as.

The Mach-Zehnder interferometer described in section 2 is placed inside the XUV arm of the main interferometer to generate a phase-locked pair of NIR pulses. These pulses are focused into a 3 mm long gas cell (GC) by a spherical mirror ($f = 750$ mm) in order to generate attosecond XUV pulses via HHG. For the following experiments argon gas at a pressure of 40 mbar is used. To ensure that the two XUV pulses are identical the ionization of the medium by the first pulse has to be controlled. We keep the intensity below 1×10^{14} W/cm^2 [47]. After recombination the XUV and NIR beams are collinear. The XUV focus and a focus generated in the NIR arm are both $2f - 2f$ re-imaged into the velocity map imaging (VMI) spectrometer chamber by a gold-coated toroidal mirror. A neutral gas medium (helium for this experiment) is supplied as target through a piezo nozzle integrated into the repeller electrode of the VMI spectrometer [48]. The gas jet is pulsed and synchronized to the laser repetition rate of 1 kHz. The polarization of the XUV and NIR pulses are in the plane of the MCP detector. After ionization either ions or electrons can be detected with a micro-channel plate (MCP) + phosphor screen detector. VMI images are recorded by a USB3 CMOS camera (ace acA2440-75um, Basler AG). Downstream from the VMI chamber a flat field XUV spectrometer [49] equipped with a variable line-spacing grating (VLG, 001-0640, Hitachi) allows for the detection of the generated XUV spectra. In Fig. 3(b) and (c) the XUV spectrum is shown for two values of the XUV-XUV delay. The spectra exhibit a modulation with a fringe period of $\delta\omega = 2\pi/\tau_{\text{XUV-XUV}}$. The fringe contrast is reduced
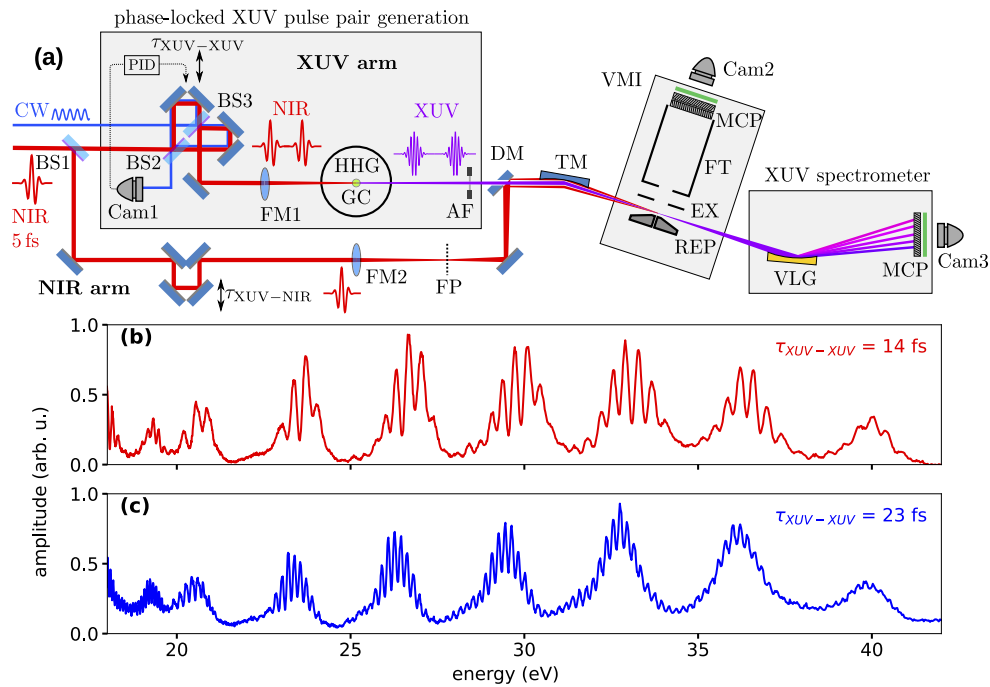
Fig. 3. Experimental setup for the generation and use of phase-locked attosecond pulse pairs. (a) Overview: The few-cycle NIR laser beam is split into an NIR and an XUV arm by beamsplitter BS1 and recombined with a drilled mirror DM. The Mach-Zehnder interferometer described in section 2 and Fig. 1 is placed inside the XUV arm of the main interferometer to create a pair of phase-locked NIR pulses, which are used for attosecond XUV pulse generation via HHG in gas cell GC. FM1 is a spherical mirror focusing the NIR pulses into the HHG chamber, FM2 is a spherical mirror focusing the probe NIR beam into the vacuum chamber (FP focal plane). Both the XUV pulse pair, and the NIR probe pulse are re-imaged into the experimental chamber with a toroidal mirror TM. Photoelectron or -ion momentum spectra can be acquired using a VMI spectrometer (REP repeller electrode, EX extractor electrode, FT flight tube, MCP micro-channel plates), and XUV photon spectra can be recorded by an XUV flat-field grating spectrometer (VLG variable line spacing grating). (b) and (c) XUV spectra for two settings of the delay $\tau_{\text{XUV-XUV}}$.

by the limited resolution of the spectrometer, which is approximately 25 meV at a photon energy of 12.36 eV [50], and lower for higher photon energies.

After HHG using the phase-locked NIR pulse pairs, a series of XUV spectra is acquired at a delay of $\tau_{\text{XUV-XUV}}$ = 26.5 fs (cf. Figure 4(a)). For each harmonic the phase of the spectral intensity modulation and therefore the XUV-XUV delay $\tau_{\text{XUV-XUV}}$ is extracted using the Takeda algorithm. The retrieved delay values for each of the harmonics 17 to 27 are shown in Fig. 4(b). As expected, the delay values follow the same dynamics for all harmonics. The standard deviations are σ = 5.7, 5.9, 7.4, 5.7, 6.9, 5.5 as, respectively. The average delay jitter taking into account the extracted delay data for all harmonics is found to be $\sigma = (6.2 \pm 0.7)$ as. As the HHG spectra are integrated over 50 shots and sampled at a lower acquisition rate compared to the data shown in Fig. 2 a direct comparison with this data is not meaningful. However, this 'out of loop' measurement confirms the phase locking of the XUV pulse pair.
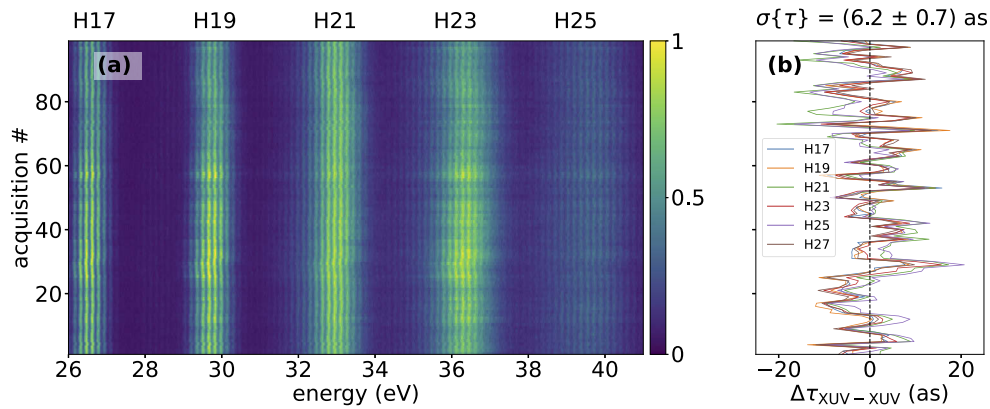
Fig. 4. XUV optical measurement of the XUV pulse pair phase stability. (a) XUV spectra with the time delay of the two XUV pulses set to $\tau_{\text{XUV-XUV}} = 26.5$ fs for a series of 100 sequential acquisitions over 5 secs. The delay jitter was evaluated for each harmonic separately using the Takeda algorithm. (b) Delay jitter evaluated for each harmonic.

4. Excitation of the Rydberg states of helium

In order to determine both the long term stability and the accuracy of our pulse pair interferometer over large delay ranges, we retrieve the energies of Rydberg states of helium by performing a Fourier-transform spectroscopy experiment. Since the energies of the Rydberg states of helium are extremely well known they permit a good physical validation of the absolute accuracy of our setup.

The two XUV pulses are focused into a helium gas jet in the VMI chamber. Harmonics 17 and above have enough energy to directly ionize the helium atoms. The harmonics 13 and 15 can populate a series of Rydberg states. These Rydberg states can be ionized by the NIR pulse. A schematic energy level diagram is shown in Fig. 5(a). Harmonic 13 excites the 1s2p state, which cannot be ionized by the NIR pulse, whereas harmonic 15 populates the Rydberg states above 1s4p, which are subsequently ionized by the NIR pulse. Due to the spectral modulation created by the two time-delayed XUV pulses, the spectral intensity at a chosen ω_{XUV} oscillates with $\tau_{\text{XUV-XUV}}$. This spectral intensity is maximal for time delays $\tau_{\text{XUV-XUV}} = n\pi/\omega_{\text{XUV}}$ with n an integer, and is zero at time delays $\tau_{\text{XUV-XUV}} = (n + 1/2)\pi/\omega_{\text{XUV}}$. Therefore the population of the Rydberg states oscillates with $\tau_{\text{XUV-XUV}}$. After 1 ps the excited helium atoms are ionized by the NIR probe pulse and the photoelectrons are measured using the VMI spectrometer. To limit the bandwidth of the probe pulse spectrum the NIR pulse is transmitted through a 25 nm bandwidth interference filter. VMI images recorded for 5000 laser shots are shown in Fig. 5(b) and are Abel inverted using the rBASEX method [51,52] in order to retrieve the three-dimensional (3D) electron momentum distribution shown in Fig. 5(c). The main contributions that are visible in the data are due to direct single photon ionization by the XUV pulse pair. Figure 5(d) displays a magnified view of the fringe modulation caused by the time delay $\tau_{\text{XUV-XUV}}$. Due to the decreasing resolution of the VMI towards higher energies, the fringes are only resolved for ionization by the lowest harmonics and for $\tau_{\text{XUV-XUV}} \lesssim 20$ fs. The photoelectron signal from direct single-photon ionization is not of interest to us. We are interested in the sharp lines close to the center of the VMI image, which correspond to ionization of Rydberg states by the NIR probe pulse.
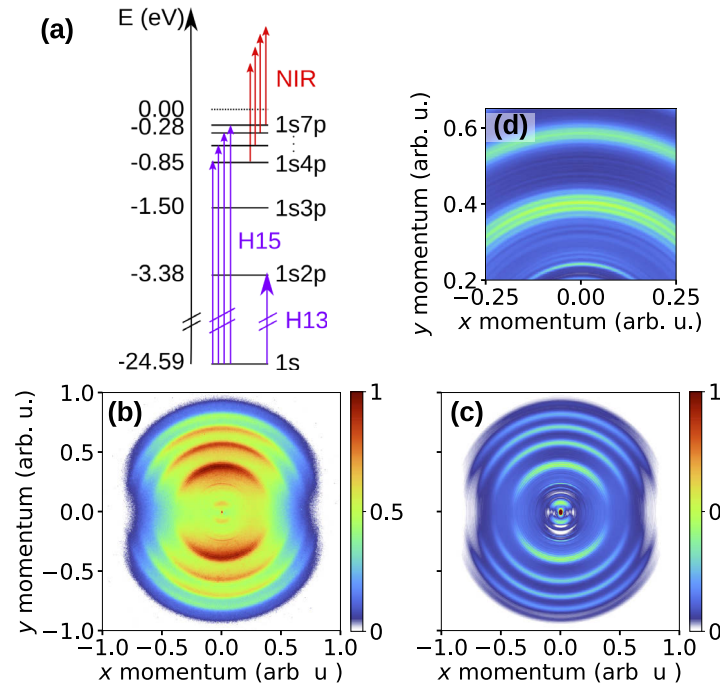
Fig. 5. (a) Schematic energy level diagram showing the Rydberg states that are populated by harmonic 13 and 15. Only the states populated by H15 are ionized by the spectrally filtered NIR pulse. (b) Electron momentum distribution recorded by velocity map imaging (VMI) spectroscopy. (c) Abel-inverted image using the rBASEX method. The image represents a slice through the retrieved 3D momentum distribution. (d) Data from (c) magnified to highlight the spectral fringe modulation of the harmonics with a fringe spacing $\delta\omega = 2\pi/\tau_{\text{XUV-XUV}}$, where $\tau_{\text{XUV-XUV}}$ is 15 fs.

To retrieve the angular distributions of the photoelectrons, the 3D photoelectron momentum distributions are expressed in terms of a series of Legendre polynomials as

$$
\begin{aligned}
P(p_{e^-}, \tau_{\text{XUV-XUV}}, \cos\theta) = \beta_0(p_{e^-}, \tau_{\text{XUV-XUV}}) \times \\
\{1 + \beta_2(p_{e^-}, \tau_{\text{XUV-XUV}})P_2(\cos\theta) + \\
\beta_4(p_{e^-}, \tau_{\text{XUV-XUV}})P_4(\cos\theta)\},
\end{aligned}
\tag{1}
$$

where θ is the angle between the photoelectron momentum p_{e^-} and the XUV+NIR polarization axis, and $\tau_{\text{XUV-XUV}}$ is the XUV-XUV time delay. $\beta_0(p_{e^-}, \tau_{\text{XUV-XUV}})$ describes the particle velocity distribution and $\beta_{2,4}(p_{e^-}, \tau_{\text{XUV-XUV}})$ describes the angular distributions of the photoelectrons [53]. Since the photoelectrons from the Rydberg states are produced by a two-photon process, the signal can be fully described by $\beta_n(p_{e^-}, \tau_{\text{XUV-XUV}})$ with $n = 0, 2, 4$.

In Fig. 6(a)-(c) $\beta_0(p_{e^-}, \tau_{\text{XUV-XUV}})$, $\beta_2(p_{e^-}, \tau_{\text{XUV-XUV}})$, and $\beta_4(p_{e^-}, \tau_{\text{XUV-XUV}})$ are shown as a function of the photoelectron momentum (in arbitrary units) and the XUV-XUV delay. One can clearly recognize the photolines of the 1s4p, 1s5p, 1s6p, and the 1s7p Rydberg states. The intensities of these photoelectron signals from the different Rydberg states oscillate with the XUV-XUV delay.

In Fig. 6(d)-(f) the corresponding Fourier transform power spectra are shown. The FT power spectrum has pronounced peaks at the photoelectron momenta corresponding to the different Rydberg states and appear around a Fourier frequency of 24 eV. As expected, there is a 1-to-1 correspondence between the Rydberg excitation energy and the measured photoelectron
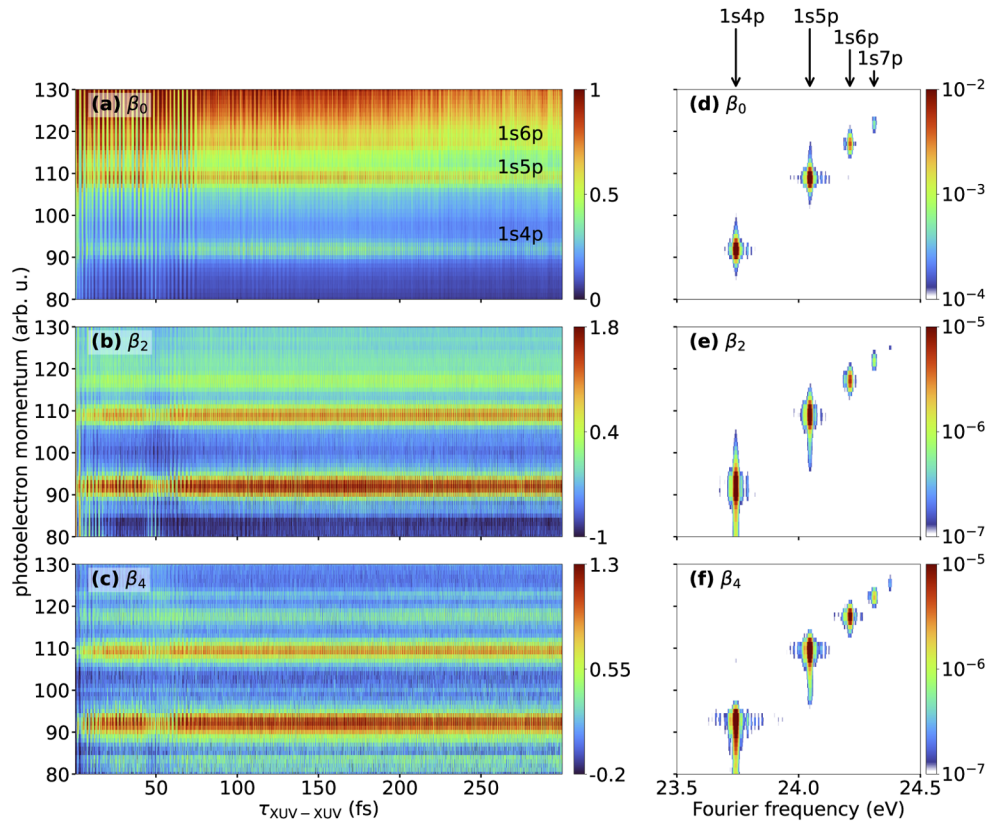
Fig. 6. (a)-(c) $\beta(p_{e^-}, \tau_{\text{XUV-XUV}})$-parameters obtained by Abel inversion of the raw VMI images, as a function of $\tau_{\text{XUV-XUV}}$ and photoelectron momentum. (d)-(e) Fourier transform power spectra corresponding to the scans in the left column. The FT power spectra contain a number of peaks that can be assigned to atomic transitions in the helium atom (see top), see Table 1 for details.

Table 1. Comparison of the Fourier frequencies of the Rydberg states of helium obtained from the experimental data and the corresponding literature values [54].

Rydberg state	Fourier frequency (eV)	FWHM (meV)	Literature value [54] (eV)
1s4p	23.7423 ± 0.0004	15.18 ± 0.27	23.7421
1s5p	24.0459 ± 0.0003	14.55 ± 0.04	24.0458
1s6p	24.2105 ± 0.0001	14.47 ± 0.08	24.2110
1s7p	24.3096 ± 0.0009	14.39 ± 0.56	24.3107

momentum. It should be noted that the FFT power spectra of all $\beta(p_{e^-}, \tau_{\text{XUV-XUV}})$ parameters agree very well, confirming that the photoelectrons originating in the Rydberg states are ionized by a two-photon process.

Figure 7 shows the normalized momentum-integrated FFT power spectrum. The spectrum is dominated by the aforementioned four strong peaks (cf. Figure 7(a)), which correspond to different Rydberg states, and which occur at Fourier frequencies that are in good agreement with literature values [54] (see in Table 1). As the exact wavelength λ_{cw} of the blue cw laser was not exactly known prior to the experiment, this wavelength is determined by minimizing the chi-squared deviations of the experimentally found peaks from the literature values. In this way

λ_{cw} is found to be 473.36 nm. The error bars for all peak positions and widths given in Table 1 are determined as the standard deviation of the data for the different $\beta_n(p_{e^-}, \tau_{XUV-XUV})$ parameters. The widths of the Rydberg peaks are found to be 14.39 to 15.19 meV in our experiment. This agrees well with the expected width of 14.8 meV due to the time delay range of our Fourier scan of 280 fs. The absolute accuracy of the delay axis in our setup can be determined as the mean of the deviations of the experimentally determined energies of the Rydberg states from the literature values, and is found to be 0.002 %.
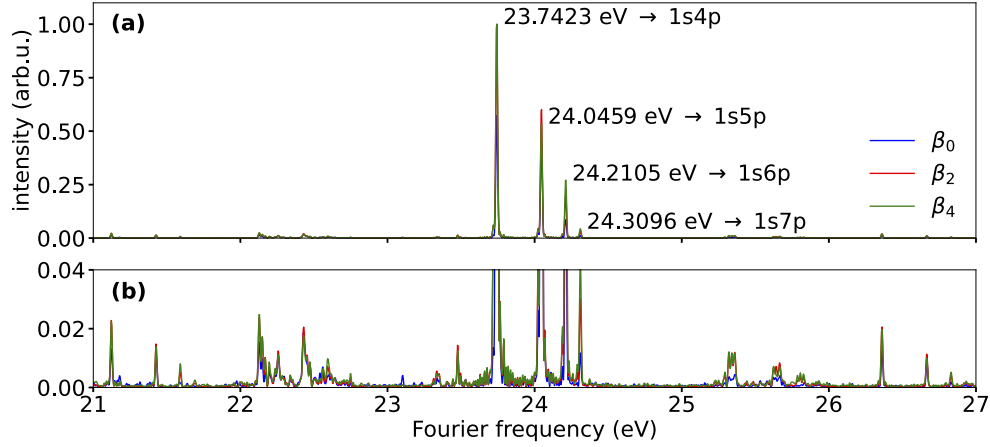

Fig. 7. (a) Normalized Fourier transform spectrum of the Rydberg states. (b) Magnified view of the power spectrum to highlight the artifact peaks, which are ± 1.6 eV and ± 2.62 eV away from the main Rydberg peaks.

In addition to the main peaks a sequence of other peaks occur in the normalized momentum-integrated FT power spectrum, which are shown in detail in Fig. 7(b). Slightly broadened replicas of the three biggest Rydberg lines 1s4p, 1s5p and 1s6p appear at energies (22.1401 ± 0.0007, 22.4417 ± 0.0004, 22.5978 ± 0.0015) eV and (25.3562 ± 0.0019, 25.6549 ± 0.0003, 25.8393 ± 0.0006) eV, respectively, displaced by (1.612 ± 0.009) eV from the Rydberg energies. This frequency difference corresponds to a good approximation of the central frequency of the NIR laser and suggests a modulation of the main signal by the NIR laser frequency. For small time delays ($\tau_{XUV-XUV} < 10$ fs) the two NIR pulses that generate the XUV pulses interfere in the focus of the HHG medium. As a consequence the total laser intensity at the focus oscillates with $\tau_{XUV-XUV}$, and along with it, the amount of generated XUV radiation [31,55]. If the two XUV pulses are generated independently, the first-order autocorrelation function of the two XUV pulses is given by

$$S^{(1)}(\tau_{XUV-XUV}) = \int_{-\infty}^{+\infty} \left| E_{XUV}(t) + E_{XUV}(t - \tau_{XUV-XUV}) \right|^2 dt, \qquad (2)$$

where $E_{XUV}(t)$ is the electric field of the XUV pulse. However, since the XUV fields are generated by HHG driven by two NIR pulses, this expression needs to be modified, and can be approximated as

$$S^{(1)}(\tau_{XUV-XUV}) = \int_{-\infty}^{+\infty} \left| \left(E_{NIR}(t) + E_{NIR}(t - \tau_{XUV-XUV}) \right)^q \right|^2 dt, \qquad (3)$$

with the electric field of the NIR pulse $E_{NIR}(t)$, and the effective non-linearity q. Therefore, the Fourier transform of the time-dependent amplitude of the XUV field, evaluated at the helium

transition frequency ω_R can be written as

$$S^{(1)}(\omega_R, \tau_{\text{XUV-XUV}}) = \left| \left[\int_{-\infty}^{+\infty} \left(E_{\text{NIR}}(t) + E_{\text{NIR}}(t - \tau_{\text{XUV-XUV}}) \right)^q e^{i\omega t} dt \right]_{\omega = \omega_R} \right|^2. \qquad (4)$$

Accordingly the signal $S^{(1)}(\omega_R, \tau_{\text{XUV-XUV}})$ oscillates with ω_R, and carries an additional modulation with ω_{NIR}. This ω_{NIR} signal modulation can readily be seen in the raw data presented in Fig. 6(a)-(c) at short delays. In addition, a similar modulation occurs at an XUV-XUV delay of 50 fs. This is due to interference with a small pre-pulse, that occurs 50 fs before the main pulse. These ω_{NIR}-modulations lead to the artifact peaks seen in the FFT (cf. Figure 7(b)). If the data with strong ω_{NIR}-modulation is excluded from the FFT processing, the artifact peaks disappear.

Further peaks occur at positions $(21.1262 \pm 0.0023, 21.4280 \pm 0.0004, 21.5968 \pm 0.0007)\,\text{eV}$ and $(26.3635 \pm 0.0005, 26.6689 \pm 0.0007, 26.8380 \pm 0.0014)\,\text{eV}$. These peaks also represent replicas of the Rydberg excitation peaks and are displaced from them by $(2.620 \pm 0.005)\,\text{eV}$. This corresponds to a wavelength of $(473.24 \pm 0.83)\,\text{nm}$, i.e. the wavelength of the blue cw stabilization laser used in the Mach-Zehnder interferometer. Ideally, the target delay fed into the stabilization system and the delay that is realized in the experiment, i.e. the phase inferred by the interference of the blue stabilization laser, are identical. In the experiment the target delay is converted to a phase given by the stabilization laser wavelength and fed into a PID controller. The target delay position is approached by slowly scanning over multiples of 2π of the cw laser period. Therefore, the actual delay position has a finite phase-dependent deviation from the target delay position for every delay setting, and therefore leads to artifact peaks at a distance from the main peaks corresponding to the photon energy of the stabilization laser. We note that the intensity of the artifact peaks is approximately two orders of magnitude below the corresponding main peaks. Therefore they do not compromise the utility of the setup and we conclude that the setup allows for high resolution spectroscopy with broadband attosecond pulses.

5. Conclusion

We have demonstrated the generation of phase-locked pairs of attosecond pulse trains. The delay between the XUV pulses can be varied over a 400 fs range with sub-10-as residual jitter. The stability of the setup has been evaluated optically in the visible and XUV. A Fourier transform spectroscopy experiment has been performed as an atomic physics based absolute accuracy test. The known Rydberg energies of helium have been retrieved with an absolute accuracy of 0.002 %.

As we have already shown our setup can be employed for the control of entanglement in bipartite quantum systems [36]. In this experiment we used pairs of attosecond pulse trains as a pump pulse in an XUV+NIR pump-probe experiment on the dissociative ionization of hydrogen molecules to control the vibrational coherence in the H_2^+ cation and therefore the entanglement between the photoelectron and ion. Recently, the topic of charge migration, i.e. the observation of electronic motion in molecules due to a coherent superposition of electronic states, has gained a lot of attention in attosecond molecular science [56,57]. So far the main challenge that has been identified for the observation of charge migration is fast decoherence. However, the role of photoelectron and -ion entanglement can also play a crucial role in the formation of electronic coherence [58]. This entanglement can be controlled by the time-delay between two phase-locked XUV pulses exciting the molecule as we have demonstrated for vibrational coherence [36]. Therefore, we believe that the combination of our setup with isolated attosecond pulses will enable successful observation and control of electronic coherence.

Disclosures. The authors declare no conflicts of interest.

Data availability. Data underlying the results presented in this paper are not publicly available at this time but may be obtained from the corresponding author upon reasonable request.

References

1. F. Krausz and M. Ivanov, "Attosecond physics," Rev. Mod. Phys. **81**(1), 163–234 (2009).
2. M. F. Ciappina, J. A. Pérez-Hernández, A. S. Landsman, W. A. Okell, S. Zherebtsov, B. Förg, J. Schötz, L. Seiffert, T Fennel, T. Shaaran, T. Zimmermann, A. Chacón, R. Guichard, A. Zaïr, J. W. G. Tisch, J. P. Marangos, T. Witting, A Braun, S. A. Maier, L. Roso, M. Krüger, P. Hommelhoff, M. F. Kling, F. Krausz, and M. Lewenstein, "Attosecond physics at the nanoscale," Rep. Prog. Phys. **80**(5), 054401 (2017).
3. J. Biegert, F. Calegari, N. Dudovich, F. Quéré, and M. J. J. Vrakking, "Attosecond technology(ies) and science," J. Phys. B: At., Mol. Opt. Phys. **54**(7), 070201 (2021).
4. P. Hamm, M. Lim, and R. M. Hochstrasser, "Structure of the Amide I Band of Peptides Measured by Femtosecond Nonlinear-Infrared Spectroscopy," J. Phys. Chem. B **102**(31), 6123–6138 (1998).
5. M. C. Asplund, M. T. Zanni, and R. M. Hochstrasser, "Two-dimensional infrared spectroscopy of peptides by phase-controlled femtosecond vibrational photon echoes," Proc. Natl. Acad. Sci. **97**(15), 8219–8224 (2000).
6. S. Mukamel, "Multidimensional Femtosecond Correlation Spectroscopies of Electronic and Vibrational Excitations," Annu. Rev. Phys. Chem. **51**(1), 691–729 (2000).
7. K. Okumura, D. M. Jonas, and Y. Tanimura, "Two-dimensional spectroscopy and harmonically coupled anharmonic oscillators," Chem. Phys. **266**(2-3), 237–250 (2001).
8. P. Tian, D. Keusters, Y. Suzaki, and W. S. Warren, "Femtosecond Phase-Coherent Two-Dimensional Spectroscopy," Science **300**(5625), 1553–1555 (2003).
9. D. M. Jonas, "Two-Dimensional Femtosecond Spectroscopy," Annu. Rev. Phys. Chem. **54**(1), 425–463 (2003).
10. T. Brixner, J. Stenger, H. M. Vaswani, M. Cho, R. E. Blankenship, and G. R. Fleming, "Two-dimensional spectroscopy of electronic couplings in photosynthesis," Nature **434**(7033), 625–628 (2005).
11. W. Kuehn, K. Reimann, M. Woerner, and T. Elsaesser, "Phase-resolved two-dimensional spectroscopy based on collinear n-wave mixing in the ultrafast time domain," J. Chem. Phys. **130**(16), 164503 (2009).
12. J. Bredenbeck, A. Ghosh, H.-K. Nienhuys, and M. Bonn, "Interface-Specific Ultrafast Two-Dimensional Vibrational Spectroscopy," Acc. Chem. Res. **42**(9), 1332–1342 (2009).
13. P. Hamm and M. Zanni, *Concepts and Methods of 2D Infrared Spectroscopy* (Cambridge University Press, 2011).
14. H. J. B. Marroux, A. P. Fidler, D. M. Neumark, and S. R. Leone, "Multidimensional spectroscopy with attosecond extreme ultraviolet and shaped near-infrared pulses," Sci. Adv. **4**(9), eaau3783 (2018).
15. E. Goulielmakis, G. Nersisyan, N. A. Papadogiannis, D. Charalambidis, G. D. Tsakiris, and K. Witte, "A dispersionless Michelson interferometer for the characterization of attosecond pulses," Appl. Phys. B: Lasers Opt. **74**(3), 197–206 (2002).
16. Y. Nabekawa, T. Shimizu, Y. Furukawa, E. J. Takahashi, and K. Midorikawa, "Interferometry of Attosecond Pulse Trains in the Extreme Ultraviolet Wavelength Region," Phys. Rev. Lett. **102**(21), 213904 (2009).
17. P. Tzallas, D. Charalambidis, N. A. Papadogiannis, K. Witte, and G. D. Tsakiris, "Direct observation of attosecond light bunching," Nature **426**(6964), 267–271 (2003).
18. T. Okino, Y. Furukawa, T. Shimizu, Y. Nabekawa, K. Yamanouchi, and K. Midorikawa, "Nonlinear Fourier transformation spectroscopy of small molecules with intense attosecond pulse train," J. Phys. B: At., Mol. Opt. Phys. **47**(12), 124007 (2014).
19. Y. Nabekawa, Y. Furukawa, T. Okino, A. Amani Eilanlou, E. J. Takahashi, K. Yamanouchi, and K. Midorikawa, "Sub-10-fs control of dissociation pathways in the hydrogen molecular ion with a few-pulse attosecond pulse train," Nat. Commun. **7**(1), 12835 (2016).
20. D. Fabris, T. Witting, W. A. Okell, D. J. Walke, P. Matia-Hernando, J. Henkel, T. R. Barillot, M. Lein, J. P. Marangos, and J. W. G. Tisch, "Synchronized pulses generated at 20 eV and 90 eV for attosecond pump–probe experiments," Nat. Photonics **9**(6), 383–387 (2015).
21. T. R. Barillot, P. Matia-Hernando, D. Greening, D. J. Walke, T. Witting, L. J. Frasinski, J. P. Marangos, and J. W. G. Tisch, "Towards XUV pump-probe experiments in the femtosecond to sub-femtosecond regime: New measurement of the helium two-photon ionization cross-section," Chem. Phys. Lett. **683**, 38–42 (2017).
22. P. Tzallas, E. Skantzakis, L. a. A. Nikolopoulos, G. D. Tsakiris, and D. Charalambidis, "Extreme-ultraviolet pump–probe studies of one-femtosecond-scale electron dynamics," Nat. Phys. **7**(10), 781–784 (2011).
23. O. Faucher, P. Tzallas, E. P. Benis, J. Kruse, A. Peralta-Conde, C. Kalpouzos, and D. Charalambidis, "Four-dimensional investigation of the 2nd order volume autocorrelation technique," Appl. Phys. B **97**(2), 505–510 (2009).
24. J. Köhler, M. Wollenhaupt, T. Bayer, C. Sarpe, and T. Baumert, "Zeptosecond precision pulse shaping," Opt. Express **19**(12), 11638–11653 (2011).
25. A. Monmayrant, S. Weber, and B. Chatel, "A newcomer's guide to ultrashort pulse shaping and characterization," J. Phys. B: At., Mol. Opt. Phys. **43**(10), 103001 (2010).
26. Y. Meng, C. Zhang, C. Marceau, A. Y. Naumov, P. B. Corkum, and D. M. Villeneuve, "Octave-spanning hyperspectral coherent diffractive imaging in the extreme ultraviolet range," Opt. Express **23**(22), 28960–28969 (2015).
27. G. S. M. Jansen, D. Rudolf, L. Freisem, K. S. E. Eikema, and S. Witte, "Spatially resolved Fourier transform spectroscopy in the extreme ultraviolet," Optica **3**(10), 1122–1125 (2016).

28. J. Tross, G. Kolliopoulos, and C. A. Trallero-Herrero, "Self referencing attosecond interferometer with zeptosecond precision," Opt. Express **27**(16), 22960–22969 (2019).

29. M. Bellini, C. Lyngå, A. Tozzi, M. B. Gaarde, T. W. Hänsch, A. L'Huillier, and C.-G. Wahlström, "Temporal Coherence of Ultrashort High-Order Harmonic Pulses," Phys. Rev. Lett. **81**(2), 297–300 (1998).

30. D. Descamps, C. Lyngå, J. Norin, A. L'Huillier, C.-G. Wahlström, J.-F. Hergott, H. Merdji, P. Saliéres, M. Bellini, and T. W. Hänsch, "Extreme ultraviolet interferometry measurements with high-order harmonics," Opt. Lett. **25**(2), 135–137 (2000).

31. M. Kovačev, S. V. Fomichev, E. Priori, Y. Mairesse, H. Merdji, P. Monchicourt, P. Breger, J. Norin, A. Persson, A. L'Huillier, C.-G. Wahlström, B. Carré, and P. Saliéres, "Extreme Ultraviolet Fourier-Transform Spectroscopy with High Order Harmonics," Phys. Rev. Lett. **95**(22), 223903 (2005).

32. R. Eramo, S. Cavalieri, C. Corsi, I. Liontos, and M. Bellini, "Method for High-Resolution Frequency Measurements in the Extreme Ultraviolet Regime: Random-Sampling Ramsey Spectroscopy," Phys. Rev. Lett. **106**(21), 213003 (2011).

33. A. Wituschek, L. Bruder, E. Allaria, U. Bangert, M. Binz, R. Borghes, C. Callegari, G. Cerullo, P. Cinquegrana, L. Giannessi, M. Danailov, A. Demidovich, M. Di Fraia, M. Drabbels, R. Feifel, T. Laarmann, R. Michiels, N. S. Mirian, M. Mudrich, I. Nikolov, F. H. O'Shea, G. Penco, P. Piseri, O. Plekan, K. C. Prince, A. Przystawik, P. R. Ribič, G. Sansone, P. Sigalotti, S. Spampinati, C. Spezzani, R. J. Squibb, S. Stranges, D. Uhl, and F. Stienkemeier, "Tracking attosecond electronic coherences using phase-manipulated extreme ultraviolet pulses," Nat. Commun. **11**(1), 883 (2020).

34. A. Wituschek, O. Kornilov, T. Witting, L. Maikowski, F. Stienkemeier, M. J. J. Vrakking, and L. Bruder, "Phase cycling of extreme ultraviolet pulse sequences generated in rare gases," New J. Phys. **22**(9), 092001 (2020).

35. M. J. J. Vrakking, "Control of Attosecond Entanglement and Coherence," Phys. Rev. Lett. **126**(11), 113203 (2021).

36. L.-M. Koll, L. Maikowski, L. Drescher, T. Witting, and M. J. Vrakking, "Experimental Control of Quantum-Mechanical Entanglement in an Attosecond Pump-Probe Experiment," Phys. Rev. Lett. **128**(4), 043201 (2022).

37. D. R. Austin, T. Witting, C. A. Arrell, F. Frank, A. S. Wyatt, J. P. Marangos, J. W. Tisch, and I. A. Walmsley, "Lateral shearing interferometry of high-harmonic wavefronts," Opt. Lett. **36**(10), 1746–1748 (2011).

38. O. Smirnova, Y. Mairesse, S. Patchkovskii, N. Dudovich, D. Villeneuve, P. Corkum, and M. Y. Ivanov, "High harmonic interferometry of multi-electron dynamics in molecules," Nature **460**(7258), 972–977 (2009).

39. S. Beaulieu, E. Bloch, L. Barreau, A. Comby, D. Descamps, R. Géneaux, F. Légaré, S. Petit, and Y. Mairesse, "Phase-resolved two-dimensional spectroscopy of electronic wave packets by laser-induced XUV free induction decay," Phys. Rev. A **95**(4), 041401 (2017).

40. D. Azoury, O. Kneller, S. Rozen, B. D. Bruner, A. Clergerie, Y. Mairesse, B. Fabre, B. Pons, N. Dudovich, and M. Krüger, "Electronic wavefunctions probed by all-optical attosecond interferometry," Nat. Photonics **13**(1), 54–59 (2019).

41. A. González-Castrillo, F. Martín, and A. Palacios, "Quantum state holography to reconstruct the molecular wave packet using an attosecond XUV–XUV pump-probe technique," Sci. Rep. **10**(1), 12981 (2020).

42. M. Takeda, H. Ina, and S. Kobayashi, "Fourier-transform method of fringe-pattern analysis for computer-based topography and interferometry," J. Opt. Soc. Am. **72**(1), 156 (1982).

43. A. Suda, M. Hatayama, K. Nagasaka, and K. Midorikawa, "Generation of sub-10-fs, 5-mJ-optical pulses using a hollow fiber with a pressure gradient," Appl. Phys. Lett. **86**(11), 111116 (2005).

44. V. Pervak, I. Ahmad, M. K. Trubetskov, A. V. Tikhonravov, and F. Krausz, "Double-angle multilayer mirrors with smooth dispersion characteristics," Opt. Express **17**(10), 7943–7951 (2009).

45. F. Silva, M. Miranda, B. Alonso, J. Rauschenberger, V. Pervak, and H. Crespo, "Simultaneous compression, characterization and phase stabilization of GW-level 14 cycle VIS-NIR femtosecond pulses using a single dispersion-scan setup," Opt. Express **22**(9), 10181 (2014).

46. H. Timmers, Y. Kobayashi, K. F. Chang, M. Reduzzi, D. M. Neumark, and S. R. Leone, "Generating high-contrast, near single-cycle waveforms with third-order dispersion compensation," Opt. Lett. **42**(4), 811–814 (2017).

47. P. Saliéres, L. Le Déroff, T. Auguste, P. Monot, P. d'Oliveira, D. Campo, J.-F. Hergott, H. Merdji, and B. Carré, "Frequency-Domain Interferometry in the XUV with High-Order Harmonics," Phys. Rev. Lett. **83**(26), 5483–5486 (1999).

48. O. Ghafur, W. Siu, P. Johnsson, M. F. Kling, M. Drescher, and M. J. J. Vrakking, "A velocity map imaging detector with an integrated gas injection system," Rev. Sci. Instrum. **80**(3), 033110 (2009).

49. T. Kita, T. Harada, N. Nakano, and H. Kuroda, "Mechanically ruled aberration-corrected concave gratings for a flat-field grazing-incidence spectrograph," Appl. Opt. **22**(4), 512–513 (1983).

50. L. Drescher, O. Kornilov, T. Witting, V. Shokeen, M. J. J. Vrakking, and B. Schütte, "Extreme-ultraviolet spectral compression by four-wave mixing," Nat. Photonics **15**(4), 263–266 (2021).

51. D. D. Hickstein, S. T. Gibson, R. Yurchak, D. D. Das, and M. Ryazanov, "A direct comparison of high-speed methods for the numerical Abel transform," Rev. Sci. Instrum. **90**(6), 065115 (2019).

52. M. Ryazanov, "Development and implementation of methods for sliced velocity map imaging. Studies of overtone-induced dissociation and isomerization dynamics of hydroxymethyl radical (CH_2OH and CD_2OH)," Ph.D. thesis, University of Southern California, Los Angeles (2012).

53. K. L. Reid, "Photoelectron angular distributions," Annu. Rev. Phys. Chem. **54**(1), 397–424 (2003).

54. D. C. Morton, Q. Wu, and G. W. Drake, "Energy levels for the stable isotopes of atomic helium (^{4}He I and ^{3}He I)," Can. J. Phys. **84**(2), 83–105 (2006).

55. N. A. Papadogiannis, E. Hertz, C. Kalpouzos, and D. Charalambidis, "Laser-intensity effects in high-order autocorrelation calculations," Phys. Rev. A **66**(2), 025803 (2002).

56. J. Breidbach and L. S. Cederbaum, "Migration of holes: Formalism, mechanisms, and illustrative applications," J. Chem. Phys. **118**(9), 3983–3996 (2003).

57. F. Remacle and R. D. Levine, "An electronic time scale in chemistry," Proc. Natl. Acad. Sci. **103**(18), 6793–6798 (2006).

58. M. Ruberti, "Onset of ionic coherence and ultrafast charge dynamics in attosecond molecular ionisation," Phys. Chem. Chem. Phys. **21**(32), 17584–17604 (2019).